The Astrophysical Journal, 972:21 (11pp), 2024 September 1 https://doi.org/10.3847/1538-4357/ad59a6


# TeV Analysis of a Source-rich Region with the HAWC Observatory: Is HESS J1809-193 a Potential Hadronic PeVatron?

A. Albert[1], R. Alfaro[2], C. Alvarez[3], J. C. Arteaga-Velázquez[4], D. Avila Rojas[2], R. Babu[5,6], E. Belmont-Moreno[2], A. Bernal[7], M. Breuhaus[8], K. S. Caballero-Mora[3], T. Capistrán[7], A. Carramiñana[9], S. Casanova[10], J. Cotzomi[11], E. De la Fuente[12], D. Depaoli[8], N. Di Lalla[13], R. Diaz Hernandez[9], B. L. Dingus[1], M. A. DuVernois[14], C. Espinoza[2], K. L. Fan[15], K. Fang[14], B. Fick[5], N. Fraija[7], J. A. García-González[16], F. Garfias[7], A. Gonzalez Muñoz[2], M. M. González[7], J. A. Goodman[15], S. Groetsch[5], J. P. Harding[1], S. Hernández-Cadena[2], I. Herzog[6], D. Huang[15], F. Hueyotl-Zahuantitla[3], P. Hüntemeyer[5], A. Iriarte[7], V. Joshi[17], S. Kaufmann[18], A. Lara[19], J. Lee[20], H. León Vargas[2], A. L. Longinotti[7], G. Luis-Raya[18], K. Malone[1], J. Martínez-Castro[21], J. A. Matthews[22], P. Miranda-Romagnoli[23], J. A. Montes[7], J. A. Morales-Soto[4], E. Moreno[11], M. Mostafá[24], L. Nellen[25], M. Newbold[26], M. U. Nisa[6], R. Noriega-Papaqui[23], M. Osorio[7], Y. Pérez Araujo[2], E. G. Pérez-Pérez[18], C. D. Rho[27], D. Rosa-González[9], E. Ruiz-Velasco[8], H. Salazar[11], A. Sandoval[2], M. Schneider[15], J. Serna-Franco[2], A. J. Smith[15], Y. Son[20], R. W. Springer[26], O. Tibolla[18], K. Tollefson[6], I. Torres[9], R. Torres-Escobedo[28], R. Turner[5], F. Ureña-Mena[9], E. Varela[11], X. Wang[5], I. J. Watson[20], E. Willox[15], S. Yun-Cárcamo[15], and H. Zhou[28]
(THE HAWC COLLABORATION)

[1] Physics Division, Los Alamos National Laboratory, Los Alamos, NM, USA
[2] Instituto de F'isica, Universidad Nacional Autónoma de México, Ciudad de Mexico, Mexico
[3] Universidad Autónoma de Chiapas, Tuxtla Gutiérrez, Chiapas, Mexico
[4] Universidad Michoacana de San Nicolás de Hidalgo, Morelia, Mexico
[5] Department of Physics, Michigan Technological University, Houghton, MI, USA; rbabu@mtu.edu
[6] Department of Physics and Astronomy, Michigan State University, East Lansing, MI, USA
[7] Instituto de Astronom'ia, Universidad Nacional Autónoma de México, Ciudad de Mexico, Mexico
[8] Max-Planck Institute for Nuclear Physics, 69117 Heidelberg, Germany
[9] Instituto Nacional de Astrof'isica, Óptica y Electrónica, Puebla, Mexico
[10] Instytut Fizyki Jadrowej im Henryka Niewodniczanskiego Polskiej Akademii Nauk, IFJ-PAN, Krakow, Poland
[11] Facultad de Ciencias F'isico Matemáticas, Benemérita Universidad Autónoma de Puebla, Puebla, Mexico
[12] Departamento de F'isica, Centro Universitario de Ciencias Exactase Ingenierias, Universidad de Guadalajara, Guadalajara, Mexico
[13] Department of Physics, Stanford University: Stanford, CA 94305-4060, USA
[14] Department of Physics, University of Wisconsin-Madison, Madison, WI, USA
[15] Department of Physics, University of Maryland, College Park, MD, USA
[16] Tecnologico de Monterrey, Escuela de Ingeniería y Ciencias, Ave. Eugenio Garza Sada 2501, Monterrey, N.L. 64849, Mexico
[17] Erlangen Centre for Astroparticle Physics, Friedrich-Alexander-Universität Erlangen-Nürnberg, Erlangen, Germany
[18] Universidad Politecnica de Pachuca, Pachuca, Hgo, Mexico
[19] Instituto de Geof'isica, Universidad Nacional Autónoma de México, Ciudad de Mexico, Mexico
[20] University of Seoul, Seoul, Republic of Korea
[21] Centro de Investigaci'on en Computaci'on, Instituto Polit'ecnico Nacional, Mexico City, Mexico
[22] Dept of Physics and Astronomy, University of New Mexico, Albuquerque, NM, USA
[23] Universidad Autónoma del Estado de Hidalgo, Pachuca, Mexico
[24] Department of Physics, Temple University, Philadelphia, PA, USA
[25] Instituto de Ciencias Nucleares, Universidad Nacional Autónoma de Mexico, Ciudad de Mexico, Mexico
[26] Department of Physics and Astronomy, University of Utah, Salt Lake City, UT, USA
[27] Department of Physics, Sungkyunkwan University, Suwon 16419, Republic of Korea
[28] Tsung-Dao Lee Institute & School of Physics and Astronomy, Shanghai Jiao Tong University, Shanghai, People's Republic of China
*Received 2024 March 21; revised 2024 June 17; accepted 2024 June 17; published 2024 August 22*

## Abstract

HESS J1809-193 is an unidentified TeV source, first detected by the High Energy Stereoscopic System (H.E.S.S.) collaboration. The emission originates in a source-rich region that includes several supernova remnants (SNRs) and pulsars including SNR G11.1+0.1, SNR G11.0-0.0, and the young radio pulsar PSR J1809-1917. Originally classified as a pulsar wind nebula candidate, recent studies show the peak of the TeV region overlapping with a system of molecular clouds. This resulted in the revision of the original leptonic scenario to look for alternate hadronic scenarios. Marked as a potential PeVatron candidate, this region has been studied extensively by H.E.S.S. due to its emission extending up to several tens of TeV. In this work, we use 2398 days of data from the High Altitude Water Cherenkov (HAWC) observatory to carry out a systematic source search of the HESS J1809-193 region. We were able to resolve emission detected as an extended component (modelled as a symmetric Gaussian with a $1\sigma$ radius of $0^{\circ}.21$) with no clear cutoff at high energies and emitting photons up to 210 TeV. We model the multiwavelength observations for the region around HESS J1809-193 using a time-dependent leptonic model and a

lepto-hadronic model. Our model indicates that both scenarios could explain the observed data within the region of HESS J1809-193.

*Unified Astronomy Thesaurus concepts:* Gamma-ray astronomy (628); Astronomical methods (1043); Gamma-ray sources (633)

## 1. Introduction

### 1.1. Previous TeV Measurements

HESS J1809-193 was originally discovered by the High Energy Stereoscopic System (H.E.S.S.) detector in 2007 (Aharonian et al. 2007) as a part of a systematic search for very high-energy emission from energetic pulsars in the Galactic plane in the very high-energy range (up to 30 TeV). H.E.S.S. originally reported that it is an extended source with a fairly hard spectral index ($\sim$2.2) that could be possibly associated with a pulsar wind nebula (PWN) powered by the pulsar PSR J1809-1917.

HESS J1809-193 was detected by the High Altitude Water Cherenkov (HAWC) Observatory in the HAWC second source catalog of TeV sources (2HWC; Abeysekara et al. 2017) as 2HWC J1809-190 and also in the third catalog of TeV sources (3HWC; Albert et al. 2020) with the source name 3HWC J1809-190. The emission of 3HWC J1809-190 is centered at (R.A., decl.) = ($272.^\circ46$, $-19.^\circ04$) with a $16\sigma$ significance (pretrials) using 1523 days of HAWC data.

The H.E.S.S. Collaboration, in 2023, updated their observations with a total of 93.2 hr of observation time above 0.27 TeV (H.E.S.S. Collaboration et al. 2023). They were able to resolve the emission into two components: an extended Component A and a compact Component B. The extended Component A was modeled as an elongated Gaussian with a $1\sigma$ semimajor (semiminor) axis of $\sim0.^\circ62$ ($\sim0.^\circ35$), which shows a spectral cutoff at $\sim$12 TeV. Component B is modeled as a symmetric Gaussian with a $1\sigma$ radius of $\sim0.^\circ1$ modeled with a hard spectrum and shows no spectral cutoff. The location of Component B is closer to PSR J1809-1917. H.E.S.S. Collaboration et al. (2023) modeled the region using a time-dependent leptonic scenario based on three generations of electrons: a halo of "relic" electrons associated with the extended Component A, "medium-age" electrons associated with the compact Component B, and "young" electrons associated with an X-ray nebula (Anada et al. 2010).

Fermi Large Area Telescope (LAT) observations of the region, performed by Araya (2018) and H.E.S.S. Collaboration et al. (2023) using the 3FGL and 4FGL data releases, respectively, list two sources in the region. As noted in H.E.S.S. Collaboration et al. (2023), the two sources in the region are (i) 4FGL J1810.3-1925e, which is modeled as an extended source (Gaussian morphology) with a log-parabola spectral curvature model, and (ii) 4FGL J1811.5-1925 is modeled as a point source and a power-law spectral model. 4FGL J1810.3-1925e's best-fit position is closer to PSR J1809-1917 and the two H.E.S.S. components, indicating an association with the emission observed by H.E.S.S. The extension of the Fermi source ($\sigma\sim0.^\circ3$) is also comparable to the extension of the extended H.E.S.S. Component A ($\sigma\sim0.^\circ6$). 4FGL J1811.5-1925 is positionally coincident with PSR J1811-1925, which indicates the association of the source with the pulsar. Therefore the emission from this region is not considered to contribute toward the bulk emission from HESS J1809-193.

HESS J1809-193 is also reported by the Large High Altitude Air Shower Observatory (LHAASO) Collaboration in 2023 as the ultrahigh-energy source 1LHAASO J1809-1918u (Cao et al. 2024). The LHAASO WCDA array detected the region as an extended Gaussian with a $1\sigma$ radius of $\sim0.^\circ35$, with a spectral index of 2.24 between 1 and 25 TeV. The KM2A array detects the region as a point source with a $1\sigma$ radius of $\sim0.^\circ22$ as an upper limit, with a soft spectral index of 3.51, at energies above 25 TeV. The source was detected by KM2A with a significance of $9.4\sigma$ at energies greater than 100 TeV, it is marked as an ultrahigh-energy source.

Recently HAWC also reported that the HESS J1809-193 region is one of the few sources emitting above 56 TeV in its high-energy source catalog (Abeysekara et al. 2020). Figure 1 shows the HAWC significance map of the region using 2398 days of data, with possible counterparts within the region. It is also noted from the catalog that there is a clear indication of emission from this region above 100 TeV with significance slightly below the threshold of confirmation ($5\sigma$). At energies above 56 TeV, the source emission remains extended with a Gaussian width of $0.^\circ34$.

The high-energy emission from similar objects is particularly intriguing to study cosmic rays near the "knee" of the cosmic-ray spectrum around 1 PeV energy. The true origin of such cosmic rays is a mystery. The acceleration process of these particles continues to be a question, given that cosmic-ray accelerators produce gamma rays near their source of origin. A fraction of the energy of these cosmic rays is transferred to gamma rays, which are detected on Earth. In this work, we will explore particle acceleration in the region using a lepto-hadronic scenario and a time-dependent leptonic scenario.

### 1.2. Multiwavelength Observations

The region in the sky in the direction of HESS J1809-193 is a source-rich region, consisting of several supernova remnants (SNR) and pulsars. The radio SNR G11.0-0.05, which is a partial-shell-type SNR, is suggested to be located at a distance of $2.4\pm0.7$ kpc (Shan et al. 2018). The radio SNR G11.1 +0.08 is also located within the TeV emission region. Both of these radio SNRs were discovered using the Karl G. Jansky Very Large Array (VLA) observations at 1465 MHz along with the Giant Metrewave Radio Telescope at 235 MHz (Brogan et al. 2004). The region also consists of a powerful high spin-down energy pulsar with a period of 82.7 ms. PSR J1809-1917, discovered by the Parkes Multibeam Pulsar Survey (Morris et al. 2002),[29] is coincident with the H.E.S.S. and HAWC peak emission locations. The X-ray diffuse emission discovered around SNR G11.0-0.08 (Bamba et al. 2003) was thought to be associated with the PWN and consequently, the TeV emission was assumed to be of a PWN origin. X-ray observations by Suzaku in the 2–10 KeV band confirmed the detection of elongated, hard, nonthermal extended emission (Anada et al. 2010). The characteristic age of PSR J1809-1917 is 51 kyr (Morris et al. 2002) while the age of the SNR G11.0-0.08 is

[29] See https://www.atnf.csiro.au/research/pulsar/psrcat/.

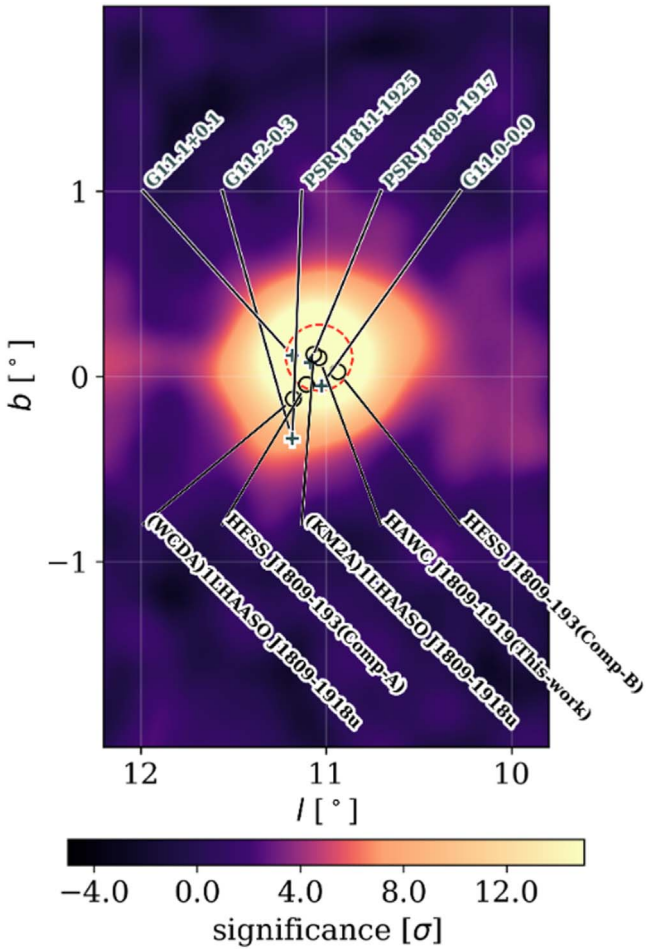


**Figure 1.** HAWC sky significance map (assuming an index of 2.7 with a point-source morphology) of the region shows the emission from HAWC J1809-1919. The distance between PSR J1809-1917 and the HAWC fit is $0.^{\circ}05 \pm 0.^{\circ}28$. The red dashed circle shows the $1\sigma$ Gaussian width of the HAWC source. The maximum significance is $27\sigma$. The upper labels show the sources in the region. The lower labels indicate the locations of the TeV sources observed by H.E.S.S., LHAASO, and HAWC (this work).

unknown, which makes the association of the pulsar to SNR G11.0-0.08 difficult. Another energetic pulsar, PSR J1811-1925 is located at the eastern edge of the TeV emission, at the center of SNR G11.2-0.3 (Manchester et al. 2005). Rangelov et al. (2014) mentioned that this pulsar and SNR along with X-ray binary XTE J1810-189 and the binary candidate Suzaku J1811-1900 are not responsible for the bulk of the observed TeV emission. This arises from the large spatial offset of PSR J1811-1925's location from the center of the emission region and XTE J1810-189 is an ordinary type I X-ray burster, and such objects have not been found to produce TeV gamma rays.

In 2016, using the expanded VLA, Castelletti et al. (2016) produced deep full-synthesis imaging at 1.4 GHz for regions near the vicinity of PSR J1809-1917. Along with $^{12}$CO observations from the James Clerk Maxwell telescope in the transition line J(3→2) and atomic hydrogen data from the Southern Galactic Plane Survey, a system of molecular clouds on the edge of the shock front of SNR G11.0-0.0 was discovered. This is spatially coincident with the peak emission of the source HESS J1809-193 although there are no radio counterparts detected for the PWN associated with PSR J1809-1917. They proposed that the most probable origin of the TeV emission comes from protons in the SNR interacting with molecular clouds in its vicinity. The density of the molecular clouds ($\sim 2-3 \times 10^3$ cm$^{-3}$) interacting with SNR G11.0-0.0 is found to be sufficient to produce the observed TeV gamma-ray emission in the region. As stated earlier, two unidentified LAT sources, 4FGL J1810.3-1925e and 4FGL J1811.5-1925 (Ballet et al. 2020) could have possible associations with the TeV source.

## 2. HAWC Observatory and Description of HAWC Data

In this analysis, we use data from the HAWC Observatory to study HESS J1809-193. The HAWC detector, located in the state of Puebla, Mexico at an altitude of 4100 m, consists of 300 water Cherenkov detector tanks and covers a total area of 22,000 m$^2$. Each tank contains four photomultiplier tubes designed to detect Cherenkov light emitted when particles travel through water at a speed greater than the speed of light in the medium. HAWC is sensitive to sources within decl. of $-26^{\circ}$ and $+64^{\circ}$ and is capable of continuously monitoring the sky with a total duty cycle of 95%.

This analysis uses 2398 days of data above 1 TeV energy, collected between 2015 June and 2022 June (Abeysekara et al. 2023). The data are binned using a 2D binning scheme of the estimated energy and the fraction of HAWC array triggered during an event as described in Abeysekara et al. (2019). The data are reconstructed using a neural network energy estimator (Abeysekara et al. 2019). This energy estimator algorithm uses artificial neural networks to estimate the energies of photons during an event based on the input parameters, which rely on air shower characteristics such as the energy deposited by the air shower in the array, the extent of the shower footprint within the detector, and the degree of attenuation of the shower by the atmosphere. The energy resolution and the angular resolution, at 10 TeV, for the neural network energy estimator at the decl. of HESS J1809-193 is ∼15% in log $E$ scale and $0.^{\circ}4$ (68% containment radius), respectively.

## 3. Modeling and Results

### 3.1. Methodology

The gamma-ray source morphology and spectrum are fit simultaneously with a multisource fitting procedure using the Multi-Mission Maximum Likelihood (3ML)[30] framework and the HAWC Accelerated Plugin[31] (Vianello et al. 2015; Abeysekara et al. 2022). The analysis is performed using a rectangular region of interest (ROI) normal to the Galactic plane and defined as $9^{\circ} < l < 13^{\circ}$ and $-4^{\circ} < b < 4^{\circ}$ where $l$ and $b$ are Galactic latitude and longitude, respectively. The data within the ROI, shown in Figure 2, are used for this analysis.

In this analysis, we used a test statistic (TS) to calculate the pretrial statistical significance of a model using the free model parameters. TS provides a statistical measure of how well an alternate hypothesis performs over a null hypothesis. TS is defined as:

$$\mathrm{TS} = 2 \ln \left( \frac{L_{\mathrm{alt}}}{L_{\mathrm{null}}} \right), \quad (1)$$

[30] https://github.com/threeML/threeML
[31] https://github.com/threeML/hawc_hal

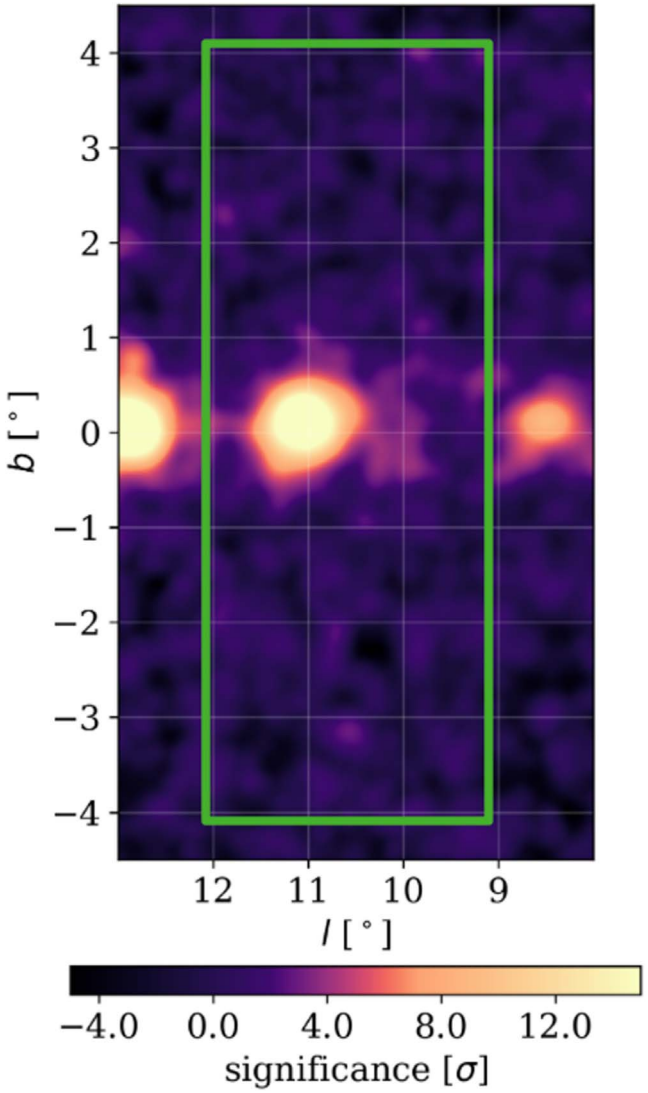


**Figure 2.** HAWC sky significance map (assuming an index of 2.7 with a point-source morphology) of the region showing the ROI in the green rectangle.

where $L_{\rm alt}$ and $L_{\rm null}$ are the likelihood values for the alternate hypothesis and null hypothesis, respectively. Using Wilks' theorem (Wilks 1938), a pretrial significance $\sigma$, which is computed as $\sigma \simeq \sqrt{\rm TS}$, is used to denote the significance of a source (alternate hypothesis) over the background (null hypothesis).

Inspired by the Fermi-LAT Extended Source Search Catalog (Ackermann et al. 2017), a source search method is carried out using a systematic multisource search analysis pipeline. The pipeline to search for point sources and extended sources within the ROI is described as follows.

1. The initial phase of the pipeline analysis involves creating a TS map for the ROI assuming point-source morphology and a spectral index of 2.7. Contributions from unresolved sources and diffuse Galactic background emissions, called the unresolved radiation model (URM), are modeled using a 2D Gaussian spatial template model centered at 0° along Galactic longitude. The URM model is fit to the data using 3ML and following the fitting process, the model is subtracted from the data. The resulting TS maps are checked for any remaining positive excess.
2. A point-source model is added to the URM model at the pixel location corresponding to the highest TS peak on the residual map. The data are then refitted using both the point-source model and the diffuse template model. If the TS between this model and the previous model (URM only) is greater than 16, then this model is chosen as the new seed model, and the residuals are examined for any positive excess. An additional point-source model is added to the new seed model at the location of the highest TS peak in the residuals, and the fitting process is repeated. This sequence is repeated until the TS of the additional point sources is less than 16 or the residual TS maps no longer show significant excess (TS $< 16$).
3. All sources, regardless of their extension, must be initially detected as a point source. Here we start checking the extension of point sources iteratively starting from the source with the maximum TS using the final point-source model as the seed model. If the difference in the TS between the extended model and the seed model is greater than 25, then the extended model becomes the seed model for the next source extension test. Throughout the extension testing phase, if the TS of any sources becomes smaller than 16, they are removed from the model. The localization, extension, and spectrum of each remaining source are refit. This process continues until the extension tests cover all the sources inside the ROI.
4. A similar approach, based on the source extension test, is adopted to test the spectra of all sources. We test the spectrum of the model using a power law (Equation (2)), a power law with an exponential cutoff (ECPL; Equation (3)), and a log-parabola spectrum (LGP; Equation (4)):

$$\phi(E) = \phi_0 \left(\frac{E}{E_0}\right)^{-\Gamma}, \tag{2}$$

$$\phi(E) = \phi_0 \left(\frac{E}{E_0}\right)^{-\Gamma} \exp\left(\frac{-E}{E_c}\right), \tag{3}$$

$$\phi(E) = \phi_0 \left(\frac{E}{E_0}\right)^{-\alpha-\beta\log\left(\frac{E}{E_0}\right)}, \tag{4}$$

where $\phi_0$ is the differential flux at a pivot energy of $E_0$, $\Gamma$ is the spectral index, $E_c$ is the cutoff energy, $\alpha$ is the spectral index, and $\beta$ is the curvature parameter for the log-parabola spectrum. The pivot energy $E_0$ used in this study is chosen as 10 TeV, to minimize correlation between the spectral parameters.

### 3.2. Results and Comparison to H.E.S.S.

The best-fit results of the source search pipeline analysis for HESS J1809-193 above 1 TeV reveal an extended source ($\sigma = 0.21 \pm 0.016$ (stat.) $\pm 0.67$ (sys.)) in the region with a symmetric Gaussian morphology located at (R.A., decl.) $= (272.^\circ38 \pm 0.^\circ021$ (stat.) $\pm 0.^\circ086$ (sys.), $-19.^\circ33 \pm 0.^\circ019$ (stat.) $\pm 0.^\circ051$ (sys.)) and a power-law spectrum with an index of $\Gamma = 2.42 \pm 0.05$ (stat.) $\pm 0.21$ (sys). The spectral energy distribution (SED) of the source is shown in Figure 4 with the corresponding data points from H.E.S.S. (H.E.S.S.

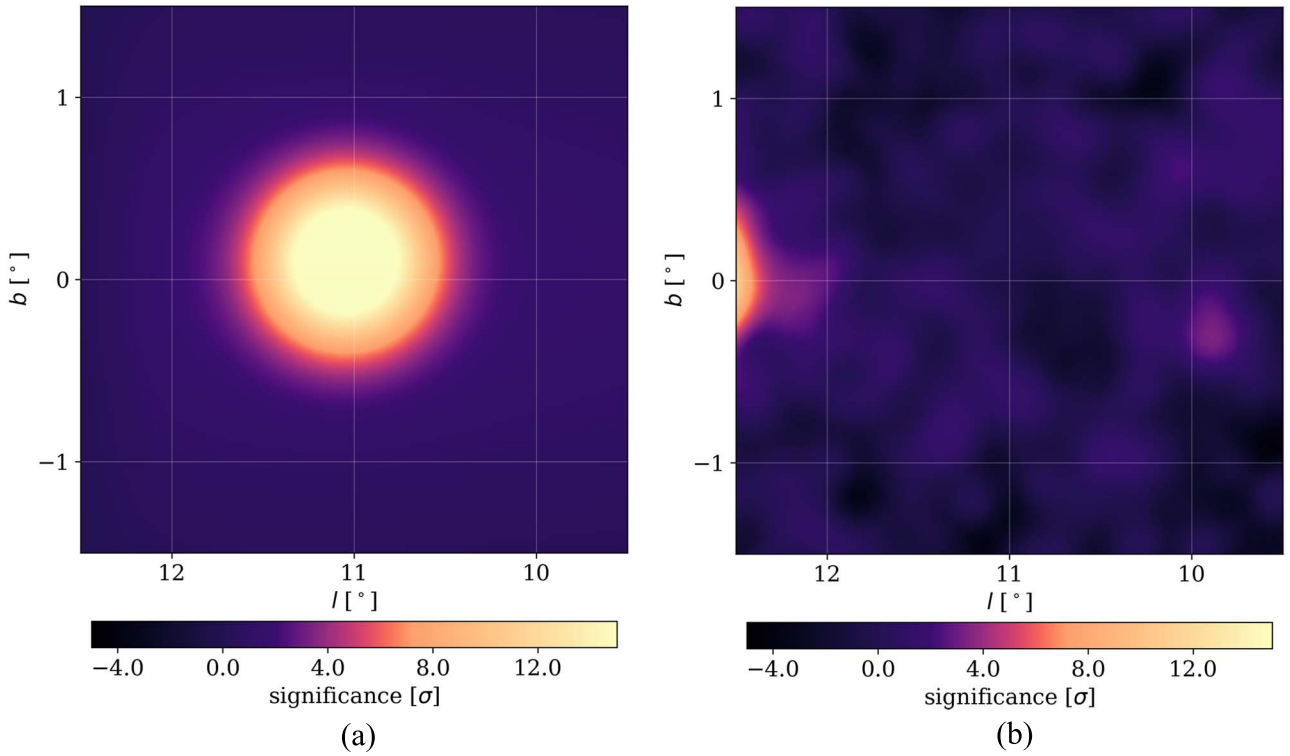


**Figure 3.** (a) A significance map of the best-fit model described in Table 1. (b) A residual map produced by subtracting the best-fit model.

Collaboration et al. 2023) and LHAASO (Cao et al. 2024). The flux points obtained from this work show signs of a potential steepening of the spectrum above 100 TeV, consistent with the spectrum observed by LHAASO above 25 TeV. Therefore we also tested the source with an ECPL model and an LGP model. We found that both complex models have a similar statistical significance, $\sim 1\sigma$ and $\sim 1.2\sigma$, respectively, compared to the power law, and are not preferred over the power-law model by $3\sigma$ significance. Therefore we adopted the simpler power-law model to best describe the region. More data at higher energies are needed to make conclusive evidence for the curvature of the spectrum.

Figure 3(a) shows a model map for the region and Figure 3(b) shows the residual map after the subtraction of the model from the data map. Table 1 shows the best-fit parameters from modeling the source at a pivot energy of 10 TeV, along with their statistical and systematic uncertainties (Abeysekara et al. 2019). Systematic uncertainties related to the modeling of the HAWC detector are investigated as described in Abeysekara et al. (2019). The effects of the detector systematic uncertainties are shown as the yellow band in Figure 4. The energy range for this source is determined by adding a step function cutoff to the best-fit model, and calculating the maximum and minimum energies with a $1\sigma$ confidence level.

The analysis was repeated using data above 56 TeV. We find that the source becomes softer above 56 TeV, with a best-fit index of $\Gamma = 2.94 \pm 0.29$ (stat.), and remains extended with a symmetric Gaussian morphology with a $1\sigma$ extension of $0.^{\circ}186 \pm 0.^{\circ}023$ (stat.). An energy-dependent morphology study for HESS J1809-193 based on the methodology explained in Section 4 of Albert et al. (2021) was done. The results of the energy-dependent morphology lacks conclusive evidence for a change in morphology with increasing energy, primarily due to the large uncertainties in the measurements attributed to the poor angular resolution of HAWC at the decl. of the source. This may be improved through additional data in the future, along with HAWC's outrigger array (Marandon et al. 2019).

**Table 1**
Best-fit Parameters and their Statistical and Systematic Uncertainties for HAWC J1809-1919

| Fit parameters | Best-fit values |
|---|---|
| TS | 392 |
| R.A. (°) | $272.38 \pm 0.021$ (stat.) $\pm 0.086$ (sys.) |
| Decl. (°) | $-19.33 \pm 0.019$ (stat.) $\pm 0.051$ (sys.) |
| $\phi_0$(TeV$^{-1}$ cm$^{-2}$ s$^{-1}$) | $3.53 \pm 0.31$ (stat.) $\pm 1.19$ (sys.) $\times 10^{-14}$ |
| Index | $2.42 \pm 0.05$ (stat.) $\pm 0.21$ (sys.) |
| $\sigma$ (°) | $0.21 \pm 0.016$ (stat.) $\pm 0.67$ (sys.) |

**Note.** $\phi_0$ is the flux normalization at a pivot energy of 10 TeV. Also given is the $1\sigma$ radius of the Gaussian morphological model

In contrast to the detection of a two-source model from H.E.S.S. (H.E.S.S. Collaboration et al. 2023; with an angular resolution of $<0.^{\circ}1$ above 1 TeV), HAWC (with an angular resolution of $0.^{\circ}55$ [68% containment radius] above 1 TeV at the decl. of HESS J1809-193), detects a single extended source, which is likely due to the different energy ranges and angular resolution of the two instruments. The comparison of spectral results suggests that the spectrum of the observed HAWC source is similar to that of the brighter component, Component A, as detected by H.E.S.S.

## 4. Spectral Modeling

Due to the number of SNRs along with potential PWNs in the region, it is unclear whether the observed gamma rays have

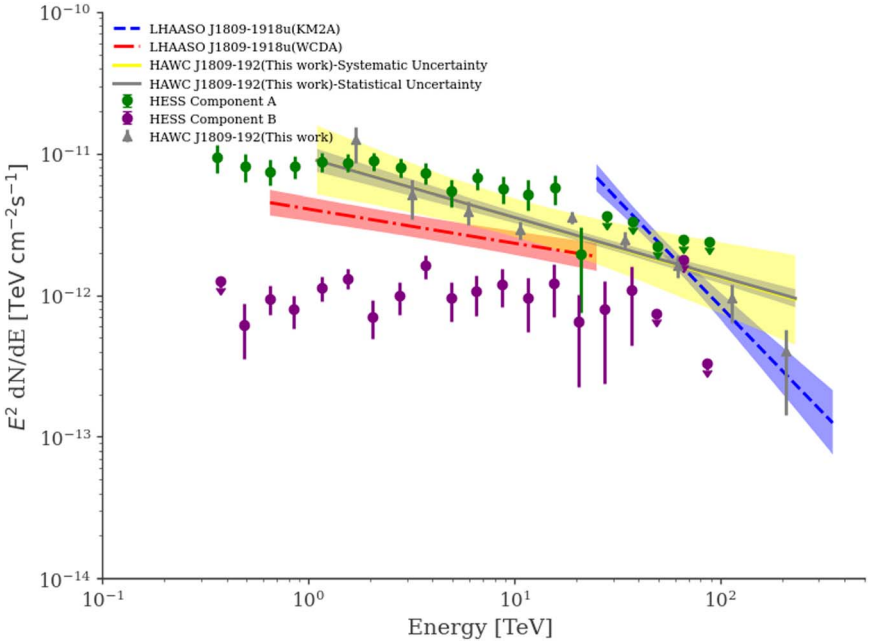


**Figure 4.** HAWC SED for HESS J1809-193. We compare the HAWC spectrum and flux points in gray triangles to spectra observed by H.E.S.S. (H.E.S.S. Collaboration et al. 2023) for the extended H.E.S.S. Component A and the compact H.E.S.S. Component B, in green and purple, respectively. The LHAASO WCDA and KM2A spectra taken from Cao et al. (2024) are shown in red and blue, respectively. HAWC spectrum (gray) shows the best-fit power-law model with the statistical uncertainties. HAWC spectrum (yellow) shows the best-fit power-law model with systematic uncertainties.

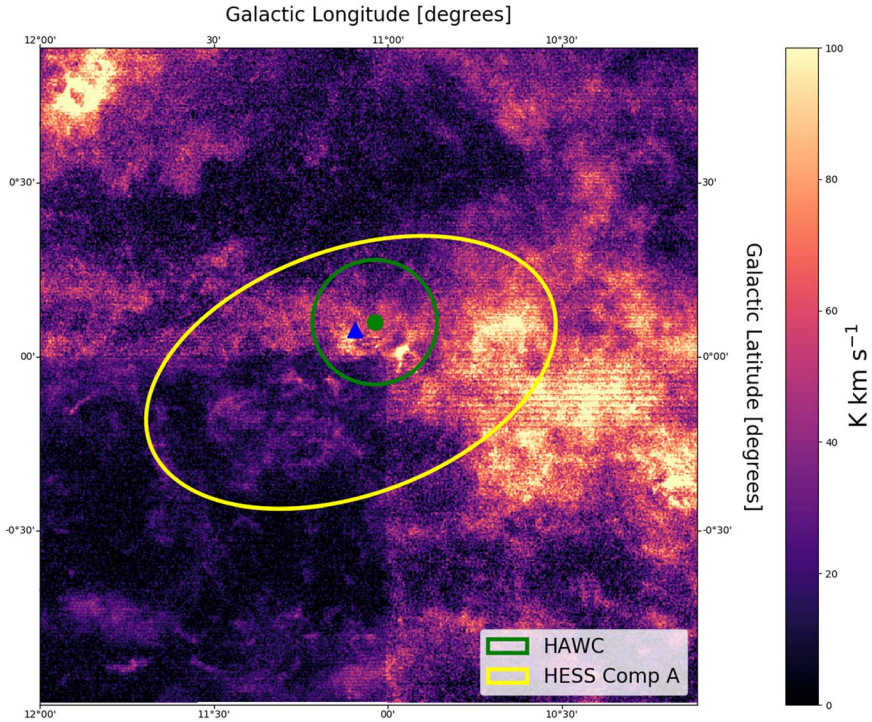


**Figure 5.** $^{12}$CO ($J = 1$–0) FUGIN line emission map (Umemoto et al. 2017) for the HESS J1809-193 region. The blue triangle represents the location of PSR J1809-1917, the green dot and circle represent the HAWC source position and the 1$\sigma$ extension, respectively, and the yellow square and ellipse represent the H.E.S.S. extended source.

a hadronic or leptonic origin. Studies performed by Castelletti et al. (2016) using $^{12}$CO data in the region of HESS J1809-193 revealed a system of molecular clouds positionally coincident with the peak of the observed gamma-ray emission from the H.E.S.S. observations. X-ray observations by Suzaku (Anada et al. 2010) reveal a hard nonthermal spectrum (photon index $\Gamma \approx 1.7$). Therefore in Section 4.1 we investigate the lepto-hadronic scenario for the multiwavelength observations from the contribution of SNR–molecular gas cloud interaction and the pulsar PSR J1809-1917 injecting particles into the system using the NAIMA (Zabalza 2015) framework. In Section 4.2, we investigate a time-dependent leptonic scenario for the PWN associated with PSR J1809-1917 using the GAMERA (Hahn et al. 2022) framework. We also note that the associations made

to the multiwavelength data are used to explain the SED alone and not the spatial features.

### 4.1. Lepto-hadronic Scenario

Observations of molecular clouds by Castelletti et al. (2016) and Voisin et al. (2019), along with the presence of SNRs, increase the probability of cosmic rays being accelerated by SNR shocks and interacting with molecular clouds in the region. Figure 5 shows $^{12}$CO ($J = 1$–0) FUGIN line emission contours overlaid with the HAWC and H.E.S.S. extensions that show the morphology of the molecular clouds detected within the region. The distance estimates for SNR G011.0-0.0, as reported in studies, include approximately 3.7 kpc according to Voisin et al. (2019), around 3.0 kpc based on Castelletti et al. (2016), $2.4 \pm 0.7$ kpc according to Shan et al. (2018), and 2.6 kpc according to Bamba et al. (2003). These estimates are closer to the distance estimate for PSR J1809-1917, which is approximately 3.7 kpc. The distance estimate for SNR G011.1 + 00.1 is 17 kpc, with a 40% fractional error (Brogan et al. 2004). This would, unrealistically, place SNR G011.1 +00.1 outside the boundaries of the Galaxy. Hence for this study, we do not consider the emissions from SNR G011.1 +00.1. Since SNR G011.0-0.0 is believed to be the progenitor of PSR J1809-1917, we show the integrated radio flux points from SNR G011.0-0.0 calculated by Brogan et al. (2006) for comparison in the multiwavelength analysis.

The H.E.S.S. detection of two components along with the break in the spectra in the GeV energy range motivates using a complex model, involving contributions from both leptonic and hadronic models (lepto-hadronic model), over a simple hadronic model. This model assumes SNR–molecular cloud interaction for the hadronic mechanism, motivated by the overlap of the HAWC data and the molecular cloud morphologies from Figure 5 (no spatial information is used in the study). For the leptonic scenario, we assume electrons are injected into the PWN by the pulsar, PSR J1809-1917. For this physical scenario, we use NAIMA to model the multi-wavelength observations.

The very high-energy gamma-ray observations from HAWC and the H.E.S.S. extended source component (Component A) are modeled with a hadronic population. Even though the molecular cloud density in the region shows a gradient (Castelletti et al. 2016), as seen in Figure 5, the TeV morphology does not show any similar characteristics across the region of HAWC J1809-1919. Therefore we calculate an average ambient density that can produce the detected TeV photons from the region. To quantify the ambient density within the region, we first calculate the gamma-ray flux for HAWC J1809-1919 above 1 TeV by taking into account the power-law spectrum of this source ($d\phi_\gamma(E)/dE = \phi_0(E/10\ \mathrm{TeV})^{-\Gamma}$), with $\phi_0$ and $\Gamma$ values from Table 1, which implies $F_\gamma(>1\ \mathrm{TeV}) = 6.4 \times 10^{-12}$ ph cm$^{-2}$ s$^{-1}$. Assuming the fraction of the total supernova explosion energy converted to cosmic-ray energies of $\theta = 10\%$ (Dermer & Powale 2013), the distance to the SNR, $d \sim 3.5$ kpc, and a supernova energy output of $10^{51}$ erg, we calculate the required ambient density in the region to produce the observed gamma-ray emission using Equation (16) of Torres et al. (2003). We find that a minimum ambient density of $n \sim 40$ cm$^{-3}$ at a distance of 3.5 kpc, is required to produce the gamma-ray emission detected above 1 TeV. This calculated value is below the density of clouds in the range of 2–3 $\times 10^3$ cm$^{-3}$ estimated by Castelletti et al. (2016), using $^{12}$CO observations.

**Table 2**
NAIMA Best-fit Parameters for the Spectral Models Shown in Figure 6

| Parameters | Best-fit Values |
|---|---|
| Leptonic fit | |
| log($A$[1/TeV]) | $43.81 \pm 1.14$ |
| $E_0$ [TeV] | 10 |
| $\Gamma_e$ | $2.49 \pm 0.06$ |
| $E_{\mathrm{cutoff}}$ [TeV] | $630.54 \pm 185$ |
| $B$-field [$\mu$G] | $2.80 \pm 0.11$ |
| $W > 1$ GeV [erg] | $2.35^{+1.19}_{-0.95} \times 10^{48}$ |
| Hadronic | |
| log($A$[1/TeV]) | $45.91 \pm 1.17$ |
| $E_0$ [TeV] | 10 |
| $\Gamma_p$ | $2.00 \pm 0.03$ |
| $E_{\mathrm{cutoff}}$ [TeV] | $349.05 \pm 65.33$ |
| $W > 1$ GeV [erg] | $1.23^{+0.09}_{-0.1} \times 10^{49}$ |

**Note.** Note that $E_0$ is fixed here.

The Suzaku X-ray observations are modeled using a leptonic population and the radio observations are used only for comparison. The X-ray flux is measured in the vicinity of the nebula (regions 2, 3, 6 and 7 in Table 4 of Anada et al. 2010). The same leptonic population can produce TeV emissions through the inverse Compton (IC) mechanism (assuming cosmic microwave background [CMB], far-infrared radiation, and near-infrared radiation photon fields as seed photons with their values set to [2.72 K, 0.261 eV cm$^{-3}$], [30 K, 0.5 eV cm$^{-3}$], and [3000 K, 1 eV cm$^{-3}$], respectively, obtained from GALPROP). We also consider the same leptonic population interacting with the molecular cloud (with an ambient ion density $n_{\mathrm{ion}} \sim 40$ cm$^{-3}$) undergoing a nonthermal bremsstrahlung process to reproduce the observed Fermi data points obtained by H.E.S.S. Collaboration et al. (2023). The parent particle spectrum is assumed to follow an ECPL, motivated by the spectrum break between LHASSO KM2A and WCDA (used only for comparison), and with an assumed distance of 3.5 kpc to the source.

The model parameters are fitted to the multiwavelength data using the Markov Chain Monte Carlo (MCMC) procedure to obtain probability distributions for the parameters of the parent particle populations. The fit parameters for the model are summarized in Table 2 and the resulting spectra are shown in Figure 6. Figure 6(a) shows the total SED for the resultant model, while Figure 6(b) shows the SED in the GeV–TeV range. WCDA and KM2A spectra from the LHAASO catalog (Cao et al. 2024) are also plotted for comparison. We observe that the total spectrum can reproduce all the observed emissions, including the highest-energy HAWC and LHAASO data.

We tested the hadronic component in NAIMA with two different maximum proton energies, $E_p$, at 800 TeV and 1 PeV, and found that a proton energy of at least 1 PeV is required to explain the TeV gamma rays. The hadronic component prefers a relatively hard index of $\Gamma_p = 2.00 \pm 0.03$ with a cutoff of 350

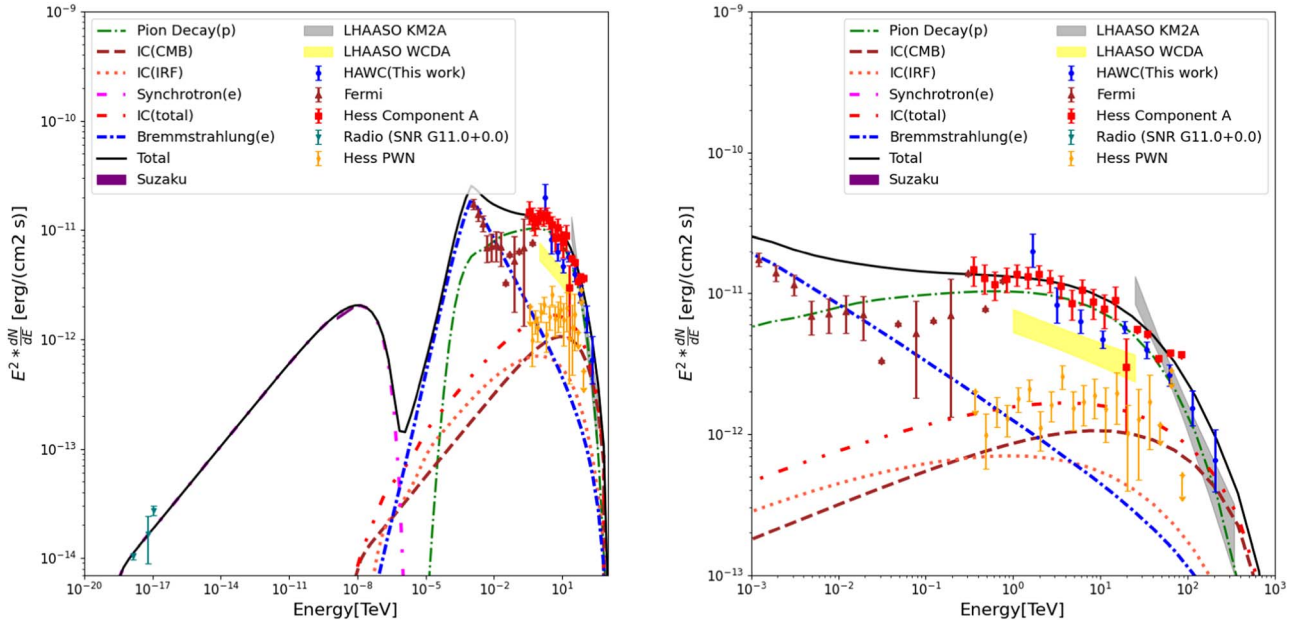


(a)Full SED (b)Zoomed-in $\gamma$-ray SED

**Figure 6.** Multiwavelength SEDs for the lepto-hadronic scenario of the HESS J1809-193 region obtained with NAIMA. The data shown include the 90 cm radio observations of SNR G11.0-0.0, with the VLA survey points in teal (Brogan et al. 2004); the Suzaku butterfly spectra in purple (Anada et al. 2010); the Fermi-LAT, H.E.S.S. Component A, and H.E.S.S. Component B flux points in brown, orange and green, respectively (H.E.S.S. Collaboration et al. 2023); and the HAWC flux points from this work in blue. Panel (a) shows the full SED for the region. The primary synchrotron component is shown in dashed pink line. The total IC SED is show in dashed red line, while the individual seed photon components for the CMB and interstellar radiation fields are shown in dashed brown and orange tomato colors, respectively. *p–p* emission is shown in green and the nonthermal bremsstrahlung emission is shown in blue dashed lines. The total SED is represented in gray. Panel (b): zoomed-in version of the SED to the gamma-ray observations. Shown for comparison, but not used in the fit, is the spectrum for the ultrahigh-energy source 1LHAASO J1809-1918u from Cao et al. (2024) and the radio flux points from SNR G11.0+0.0

TeV. Integrating the spectrum above 1 GeV gives a total proton energy of $W_p \sim 1.23 \times 10^{49}$ erg, which is a very small fraction of the calculated energy released in a supernova explosion of $\sim 10^{51}$ erg (Ginzburg & Ptuskin 1976). Considering the gas density gradient across the HAWC $1\sigma$ width of $0.^{\circ}21$ observed by FUGIN (Figure 5), cosmic rays accelerated by SNR G011.0-0.0 can potentially reach the dense molecular clouds in the region ($n_h \sim 40$ cm$^{-3}$) and produce the observed gamma rays. In the case of the *p–p* interaction scenario, the presence of a secondary synchrotron component from the secondary electrons produced in the process is expected. Observations of the region with a larger field of view with X-ray telescopes would provide evidence of such an emission.

The secondary electrons in the *p–p* scenario is not adding complexity to the model, they are just expected to be present. They need to be mentioned even though their synchrotron emission is not computed.

For the leptonic model, we get an index of $\Gamma_e = 2.49 \pm 0.06$ and a relatively low magnetic field of $B = 2.8 \pm 0.11$ $\mu$G. The synchrotron emission from the leptonic model shows good agreement with the Suzaku X-ray data. We also observe that this same population of electrons at higher energies can reproduce the spectrum of the compact component detected by H.E.S.S. (H.E.S.S. Component B) through the IC mechanism. This could explain the X-ray component along with H.E.S.S. Component B, and is compatible with the emission surrounding the PWN associated with PSR J1809-1917. The same leptonic population could interact with the molecular cloud in the vicinity undergoing the bremsstrahlung mechanism to reproduce the $\leqslant$100 GeV gamma-ray emission observed by Fermi.

### 4.2. Time-dependent Leptonic Model

In this section, we explain the spectra assuming a leptonic scenario, where the emission originates from a PWN powered by the pulsar PSR J1809-1917. The observed period ($P$) and the period time derivative ($\dot{P}$) are 82.7 ms and $2.553 \times 10^{-14}$, respectively (Manchester et al. 2005). The characteristic age, $\tau_c$, of the pulsar is 51.3 kyr, which is an estimated measure for the pulsar's age, provided the assumptions of a pulsar braking index $n = 3$ and the birth period ($P_0$) is less than the observed period $P$ hold true (Gaensler & Slane 2006). The distance used to calculate the flux in this model is assumed to be 3.5 kpc. We found that a model with a minimum of three particle populations is required describe the observed TeV and X-ray data. The radio flux data are shown only for comparison and are not included in the fit. In this model, the fraction of the pulsar spin-down luminosity converted to electrons ($\theta$ fraction), particle cutoff energy ($E_c$), and the birth period ($P_0$) are treated as unknown parameters used to describe the injected electron spectrum. The true age of the system, $\tau$, is calculated as a function of $P_0$ using Equation (5):

$$\tau = \frac{P}{(n-1)\dot{P}}\left[1 - \left(\frac{P_0}{P}\right)^{n-1}\right]. \quad (5)$$

We use the GAMERA package (Hahn et al. 2022) to model the spectrum of the radiation produced by the particles. GAMERA can produce a time-dependent model of relativistic electrons, including their injection and cooling, producing photon emission in different wavelengths. In this model we consider the ECPL form for the injected electrons. The seed radiation fields used to calculate the IC spectrum are calculated from Popescu et al. (2017) for the location of PSR J1809-1917.

**Table 3**
Pulsar Parameters and Fit Parameters for the Time-dependent Pulsar Wind Nebula Model

| Parameter | Parameter Description | Fit Values |
|---|---|---|
| | Pulsar parameters | |
| $\dot{E}$ | Spin-down power | $1.8 \times 10^{36}$ erg s$^{-1}$ |
| $\tau_c$ | Characteristic age | 51 kyr |
| $P$ | Pulsar period | 82.76 ms |
| $\dot{P}$ | Pulsar period derivative | $2.55 \times 10^{-14}$ s s$^{-1}$ |
| $d$ | Distance to pulsar | 3.3 kpc |
| $n$ | Braking index | 3 |
| | Fitting parameters | |
| $\theta$ | Power fraction | 0.67 |
| $E_c$ | Particle cutoff energy | 794 TeV |
| $\alpha$ | Particle injection index | 2.1 |
| $B$ | Magnetic field | 3.2 $\mu$G |
| $P_0$ | Pulsar birth period | 47 ms |
| $\tau_{\rm young}$ | Age of young electrons | 3.1 kyr |
| $\tau_{\rm med}$ | Age of medium-age electrons | 10.2 kyr |
| $\tau_{\rm relic}$ | Age of relic electrons | 26.5 kyr |

**Note.** The listed values are the pulsar parameters taken from ATNF catalog (Manchester et al. 2005) and the fit parameters obtained from an MCMC fit to the spectral data using GAMERA.

Gaensler & Slane (2006) specify the conditions for the time evolution for $B$, $\dot{E}$, and $P$. The time-dependent modeling approach is similar to the approach outlined in Albert et al. (2021) and H.E.S.S. Collaboration et al. (2023). The parameters of the model are described in Table 3.

We fit the model to three generations of electrons: relic, medium age, and recently injected "young electrons." Relic electrons are electrons injected into the ISM by the PWN over the lifetime of the system; in this case the result of the fit gives the age of the system as $\tau \sim 26.5$ kyr, and is associated with the HAWC, H.E.S.S. Component A, and LHAASO WCDA components. Medium-age electrons are electrons injected into the system in the last 10.2 kyr and are associated with the compact H.E.S.S. Component B. Young electrons are electrons injected into the system in the last ~3.1 kyr and are associated with the X-ray nebula. We also see that the evolved spectrum has an index of $\Gamma = 2.1$, an evolved present-day magnetic field $B \sim 3.2$ $\mu$G, and about 67% of the pulsar's spin-down luminosity is converted to electrons. This signifies that the spin-down energy of the pulsar is sufficient to maintain the energy of electrons and positrons in the wind of the pulsar powering the entire multiwavelength observations.

## 5. Discussion

The outcome from the SED modeling and analysis suggests two potential models to describe the observed multiwavelength spectra: (i) a lepto-hadronic scenario, describing the potential involvement of cosmic rays produced by the SNR and PWN or (ii) a time-dependent model, with three population of electrons injected into the ISM by the PWN system, each associated with their respective emission wavelengths (TeV gamma rays and X-rays).

In the lepto-hadronic scenario for the observed multi-wavelength SED, the protons accelerated at the shocks from SNR G11.0-0.0, SNR G11.1+0.1, or both, could be responsible for the observed GeV–TeV gamma-ray emission. While the ages of these SNRs remain unclear, measurements done based on the association of $^{12}$CO and H I self-absorption features done by Castelletti et al. (2016) places SNR G11.0-0.0 at approximately 3 kpc, within the uncertainties of the derived kinematic distance. This could indicate the association of SNR G11.0-0.0 as the progenitor of PSR J1809-1917. Protons accelerated by SNR G11.0-0.0 could interact with the molecular gas clouds in their immediate vicinity to produce the observed TeV emission. The total mass and total proton density, as measured by Castelletti et al. (2016, taking into account contributions from both H I and $^{12}$CO emissions) from the molecular clouds are estimated to be $M \approx 3 \times 10^3$ $M_\odot$ and $\eta \approx 7.4 \times 10^3$ cm$^{-3}$, respectively, which are found to fulfill the required amount of target material for hadronic interactions. We conclude that a proton energy of at least 1 PeV is required for a distance of 3.5 kpc to the source, and an average molecular cloud density of ~40 cm$^{-3}$ for proton interactions is required within the region of high-energy gamma-ray emissions for an SNR shock scenario. This could indicate that the source is a hadronic PeVatron. The estimated value of the present-day $B$-field is ~2.8 $\mu$G, which is low relative to the ISM and it depends on the normalization of the peak of the X-ray synchrotron emission. While the magnetic field is comparatively low, the synchrotron emission can explain the X-ray data. Considering the X-ray emission is produced near the PWN, the same population of electrons is also able to reproduce the TeV emission observed from the compact H.E.S.S. Component B, which is spatially coincident with the pulsar and the PWN.

For the time-dependent PWN scenario, we show SEDs obtained for three generations of electrons. The model describes well the spectra of HAWC and H.E.S.S. Component A and the X-ray flux from Suzaku. The fit yields an average present-day magnetic field of ~3.2 $\mu$G and a reasonable index for the injection spectrum of ~2.1. A maximum electron energy of several hundred TeV is also observed from the spectral fit, which is similar to the maximum electron energy observed in the lepto-hadronic fit. The model predicts that the "relic" old electrons injected into the system would cool down over time, which could explain the slight cutoff observed at the highest energies. In the case of the relic electrons, we find that the observed total synchrotron emission overshoots the observed SED by a factor of 2–3 at energies between 2–10 keV. This is potentially due to the smaller ROI (~0.°3 × 0.°3) of the Suzaku observations. Anada et al. (2010) found diffuse X-ray emission extending to the south beyond the PWN. Therefore if the origin of the TeV gamma rays is of leptonic origin, then diffuse X-ray emission from synchrotron radiation could surround the X-ray PWN with a morphology similar to the observed TeV one. Therefore to quantify the flux from this diffuse X-ray region, H.E.S.S. Collaboration et al. (2023) calculated an upper limit (95% confidence limit) for the X-ray flux, as shown in Figure 7. H.E.S.S. Collaboration et al. (2023) observed in their modeling that the synchrotron emission from relic electrons match the upper limit. Our modeling results show that the synchrotron flux produced by both relic and medium-age electrons are well below the X-ray upper limits at keV energies.

This model scenario however cannot explain the Fermi-LAT observations below ~10 GeV. This could be attributed to a secondary population of particles, undergoing a nonthermal

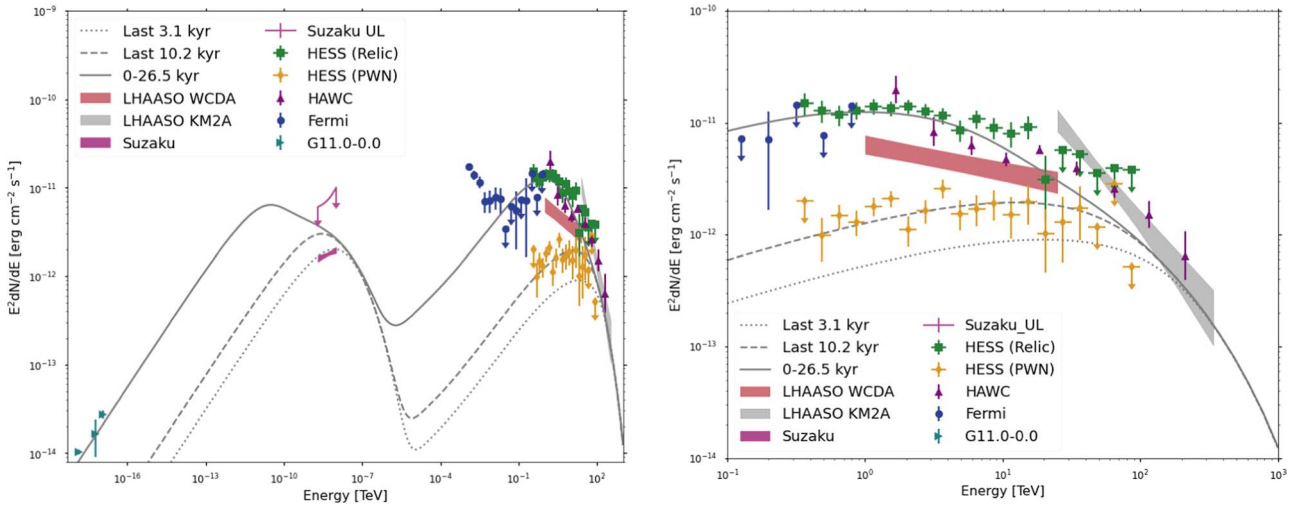


(a)Full SED (b)$\gamma$-ray SED

**Figure 7.** Multiwavelength SED for the time-dependent leptonic model of HESS J1809-193 obtained with GAMERA. The presented data are identical to the one shown in Figure 6. Panel (a) shows the full SED of the region for the three generations of electrons. The solid line indicates the old "relic" electrons. The dashed lines and curved lines correspond to the medium-age and young electrons injected into the system, respectively. Panel (b) shows a zoomed-in view of the gamma-ray observations and their MCMC results. Shown for comparison (but not used in the fit) is the spectrum of the ultrahigh-energy source 1LHAASO J1809-1918u from Cao et al. (2024).

bremsstrahlung process near the pulsar with the gas density in the region as mentioned previously.

## 6. Conclusions and Outlook

In this work, we perform a detailed spectral and morphological study of HESS J1809-193 using 2398 days of HAWC data. Unlike the H.E.S.S. observations of this region, the HAWC observations indicate a single extended source in the region and no conclusive evidence for an energy-dependent morphology due to the low angular resolution of the detector at higher zenith angles. The morphology of the region reveals an extended symmetric Gaussian source with a $1\sigma$ extension of $0.21 \pm 0.016$ (stat.) above 1 TeV and $0.^{\circ}186 \pm 0.023$ (stat.) above 56 TeV. Spectral studies indicate a power-law spectrum with an index of $\sim$2.44. There could be a potential steepening of the spectrum at the highest energies indicated by the last flux point above 200 TeV, which requires more data/statistics. The HAWC spectrum extends the emission observed by H.E.S.S. well past 56 TeV.

Studies done by H.E.S.S. Collaboration et al. (2023), have considered a time-dependent leptonic scenario to explain the multiwavelength spectrum of HESS J1809-193 by invoking electrons injected into the system by PSR J1809-1917. The lepto-hadronic model proposed by Boxi & Gupta (2024) was also used to explain the emission of HESS J1809-193, where the explosion of SNR G11.0-0.0 injected cosmic-ray protons and electrons into the region producing the high-energy gamma rays. In our studies, we have expanded on the multiwavelength model proposed by H.E.S.S. using newer HAWC data and place better constraints on the model. We also suggested that a lepton-hadronic scenario involving the SNR injecting cosmic-ray protons and the PWN produced by PSR J1809-1917 injecting cosmic-ray electrons into the system can better explain the observed high-energy gamma rays and X-rays simultaneously, except for the Fermi-LAT data below $\sim$10 GeV.

As mentioned earlier, this work is based on spectral association alone and a detailed study of spatial association is left for future studies. Hence we cannot provide conclusive evidence for the origin of the gamma rays from the region of HESS J1809-193. Conclusive evidence of gamma-ray production from the region requires deep morphological and spectral studies of the SNRs present. Future observations from LHAASO, the upcoming Cherenkov Telescope Array, and the Southern Wide-Field Gamma-Ray Observatory could provide unprecedented observations to enhance our understanding of the region.

## Acknowledgments

We acknowledge the support from: the US National Science Foundation (NSF); the US Department of Energy Office of High-Energy Physics; the Laboratory Directed Research and Development (LDRD) program of Los Alamos National Laboratory; Consejo Nacional de Ciencia y Tecnología (CONACyT), México, grants 271051, 232656, 260378, 179588, 254964, 258865, 243290, 132197, A1-S-46288, A1-S-22784, CF-2023-I-645, cátedras 873, 1563, 341, and 323, Red HAWC, México; DGAPA-UNAM grants IG101323, IN111716-3, IN111419, IA102019, IN106521, IN110621, IN110521, and IN102223; VIEP-BUAP; PIFI 2012 and 2013 and PROFOCIE 2014 and 2015; the University of Wisconsin Alumni Research Foundation; the Institute of Geophysics, Planetary Physics, and Signatures at Los Alamos National Laboratory; Polish Science Centre grant, DEC-2017/27/B/ST9/02272; Coordinación de la Investigación Científica de la Universidad Michoacana; Royal Society—Newton Advanced Fellowship 180385; Generalitat Valenciana, grant CIDEGENT/2018/034; The Program Management Unit for Human Resources & Institutional Development, Research and Innovation, NXPO (grant No. B16F630069); Coordinación General Académica e Innovación (CGAI-UdeG), PRODEP-SEP UDG-CA-499; and the Institute of Cosmic Ray Research (ICRR), University of Tokyo. H.F. acknowledges support by NASA under award number 80GSFC21M0002. We also acknowledge the significant contributions over many years of Stefan Westerhoff, Gaurang Yodh, and Arnulfo Zepeda Dominguez,

all deceased members of the HAWC collaboration. Thanks to Scott Delay, Luciano Díaz, and Eduardo Murrieta for technical support.

## ORCID iDs

R. Babu https://orcid.org/0000-0002-5529-6780
E. Belmont-Moreno https://orcid.org/0000-0003-3207-105X
M. Breuhaus https://orcid.org/0000-0003-0268-5122
K. S. Caballero-Mora https://orcid.org/0000-0002-4042-3855
D. Depaoli https://orcid.org/0000-0002-2672-4141
M. A. DuVernois https://orcid.org/0000-0002-2987-9691
A. L. Longinotti https://orcid.org/0000-0001-8825-3624
G. Luis-Raya https://orcid.org/0000-0003-2810-4867
K. Malone https://orcid.org/0000-0001-8088-400X
P. Miranda-Romagnoli https://orcid.org/0000-0002-8390-9011
F. Ureña-Mena https://orcid.org/0000-0002-2748-2527

## References

Abeysekara, A. U., Albert, A., Alfaro, R., et al. 2017, ApJ, 843, 40
Abeysekara, A. U., Albert, A., Alfaro, R., et al. 2020, PhRvL, 124, 021102
Abeysekara, A. U., Albert, A., Alfaro, R., et al. 2022, ICRC (Berlin), 37, 828
Abeysekara, A. U., Albert, A., Alfaro, R., et al. 2023, NIMPA, 1052, 168253
Abeysekara, A. U., et al. 2019, ApJ, 881, 134
Ackermann, M., Ajello, M., Baldini, L., et al. 2017, ApJ, 843, 139
Aharonian, F., Akhperjanian, A. G., Bazer-Bachi, A. R., et al. 2007, A&A, 472, 489
Albert, A., Alfaro, R., Alvarez, C., et al. 2021, ApJ, 911, 143
Albert, A., Alfaro, R., Alvarez, C., et al. 2020, ApJ, 905, 76
Anada, T., Bamba, A., Ebisawa, K., & Dotani, T. 2010, PASJ, 62, 179
Araya, M. 2018, ApJ, 859, 69
Ballet, J., Burnett, T. H., Digel, S. W., & Lott, B. 2020, ApJS, 247, 33
Bamba, A., Ueno, M., Koyama, K., & Yamauchi, S. 2003, ApJ, 589, 253
Boxi, S., & Gupta, N. 2024, ApJ, 961, 61
Brogan, C. L., Devine, K. E., Lazio, T. J., et al. 2004, AJ, 127, 355
Brogan, C. L., Gelfand, J. D., Gaensler, B. M., Kassim, N. E., & Lazio, T. J. W. 2006, ApJL, 639, L25
Cao, Z., Aharonian, F., An, Q., et al. 2024, ApJS, 271, 25
Castelletti, G., Giacani, E., & Petriella, A. 2016, A&A, 587, A71
Dermer, C. D., & Powale, G. 2013, A&A, 553, A34
Gaensler, B. M., & Slane, P. O. 2006, ARA&A, 44, 17
Ginzburg, V. L., & Ptuskin, V. S. 1976, RvMP, 48, 161
Hahn, J., Romoli, C., & Breuhaus, M., 2022 GAMERA: Source modeling in gamma astronomy, Astrophysics Source Code Library, ascl:2203.007
H.E.S.S. Collaboration, Aharonian, F., Ait Benkhali, F., et al. 2023, A&A, 672, A103
Manchester, R. N., Hobbs, G. B., Teoh, A., & Hobbs, M. 2005, AJ, 129, 1993
Marandon, V., Jardin-Blicq, A., & Schoorlemmer, H. 2019, ICRC (Madison, WI), 36, 736
Morris, D. J., Hobbs, G., Lyne, A. G., et al. 2002, MNRAS, 335, 275
Popescu, C. C., Yang, R., Tuffs, R. J., et al. 2017, MNRAS, 470, 2539
Rangelov, B., Posselt, B., Kargaltsev, O., et al. 2014, ApJ, 796, 34
Shan, S. S., Zhu, H., Tian, W. W., et al. 2018, ApJS, 238, 35
Torres, D. F., Romero, G. E., Dame, T. M., Combi, J. A., & Butt, Y. M. 2003, PhR, 382, 303
Umemoto, T., Minamidani, T., Kuno, N., et al. 2017, PASJ, 69, 78
Vianello, G., Lauer, R. J., Younk, P., et al. 2015, ICRC (The Hague), 34, 1042
Voisin, F. J., Rowell, G. P., Burton, M. G., et al. 2019, PASA, 36, e014
Wilks, S. S. 1938, Ann. Math. Stat., 9, 60
Zabalza, V. 2015, ICRC (The Hague), 34, 922